Electrical Power and Energy Systems 144 (2023) 108562

Contents lists available at ScienceDirect

International Journal of Electrical Power and Energy Systems

journal homepage: www.elsevier.com/locate/ijepes

Conductance-frequency droop control to ensure transient stability of inverter-based stand-alone microgrids☆

Joseba Erdocia [a,b,*], Andoni Urtasun [a], Luis Marroyo [a]

[a] Department of Electrical, Electronic and Communication Engineering, Public University of Navarre, Pamplona 31006, Spain
[b] Department of Photovoltaic Solar Energy, Ingeteam Power Technology S.A – Energy, Sarriguren 31621, Spain

ARTICLE INFO

Keywords:
Inverter-based microgrids
Droop control
Current limitation
Overloads
Short-circuits

ABSTRACT

Currently, inverter-based stand-alone microgrids are gaining interest due to the advantages of obtaining energy from renewable sources. To manage the operation, these microgrids include storage systems connected in parallel to the PCC through electronic inverters that are controlled as voltage sources in order to support the frequency and voltage at the PCC. For the purpose of ensuring P and Q sharing among inverters and also the synchronization stability of the microgrid, droop control is widely used, achieving a satisfactory performance in normal operation. Nevertheless, in the presence of overloads or short-circuits, the inverters must limit the current for self-protection, thereby modifying the performance of the system that then becomes prone to suffer transient stability problems. In this paper, first the performance of the inverter-based stand-alone microgrids with the conventional *P-f* and I_{act}-*f* droops is analyzed, obtaining the stability boundaries during current limitation. In order to always ensure the synchronization stability of the system, this paper then proposes the *G-f* droop that consists in employing the equivalent conductance seen by each inverter for its frequency droop control. Furthermore, as this variable always correctly represents the inverter power angle, the system dynamics are not affected by the operating conditions. The theoretical results have been validated by means of simulation and Hardware-In-the-Loop results, showing the superior performance of the proposed *G-f* droop.

1. Introduction

Traditionally, stand-alone systems have used fossil fuel-based generators to provide electricity. However, these are now being replaced by renewable generation sources and storage systems that offer a more attractive alternative in order to reduce the cost of electricity and ensure sustainable, environmentally-friendly energy production [1]. These generators are connected together through electronic inverters, giving rise to inverter-based stand-alone microgrids [2,3].

In these stand-alone systems, the parallel-connected inverters used in the storage systems are controlled as voltage sources due to the fact that they are responsible for maintaining the frequency and voltage at the point of common coupling (PCC). For this purpose, a widely used method is the control droop [4–8], which makes it possible to guarantee active and reactive power sharing among the different inverters forming part of the system, in line with their capacity. Furthermore, this control technique is performed using local measurements in each inverter and, therefore, there is no need for communication between inverters. This is of great interest due to the decentralized nature of the different systems making up the stand-alone microgrids.

Generally, droop control comprises two parallel control loops, the active power-frequency (*P-f*) droop and the reactive power-voltage (*Q-V*) droop. These are used to calculate the reference frequency and voltage that must be generated at the inverter output based on the active and reactive power measurements, respectively. This droop control is carried out under the assumption that the output impedance is inductive due to the fact that the inverters always include switching harmonic filter coils [7]. In normal conditions, i.e. with currents below the rated value, *P-f* droop makes it possible to maintain the synchronization of the inverters by providing stable performance and, at the same time, balancing the active power sharing [9,10].

However, in the event of overloads or transient short-circuits (SCs), situations in which the inverters must also remain connected, the currents exchanged by the inverters may be several times over their rated

☆ This work has been supported by the Spanish State Research Agency (AEI) under grant PID2019-110956RB-I00/AEI/ 10.13039/501100011033, and by the Public University of Navarre through a PhD scholarship. Open access funding provided by Public University of Navarre.

* Corresponding author.
E-mail address: ioseba.erdocia@unavarra.es (J. Erdocia).

https://doi.org/10.1016/j.ijepes.2022.108562
Received 12 February 2022; Received in revised form 20 July 2022; Accepted 15 August 2022
Available online 30 August 2022
0142-0615/© 2022 The Authors. Published by Elsevier Ltd. This is an open access article under the CC BY-NC-ND license (http://creativecommons.org/licenses/by-nc-nd/4.0/).

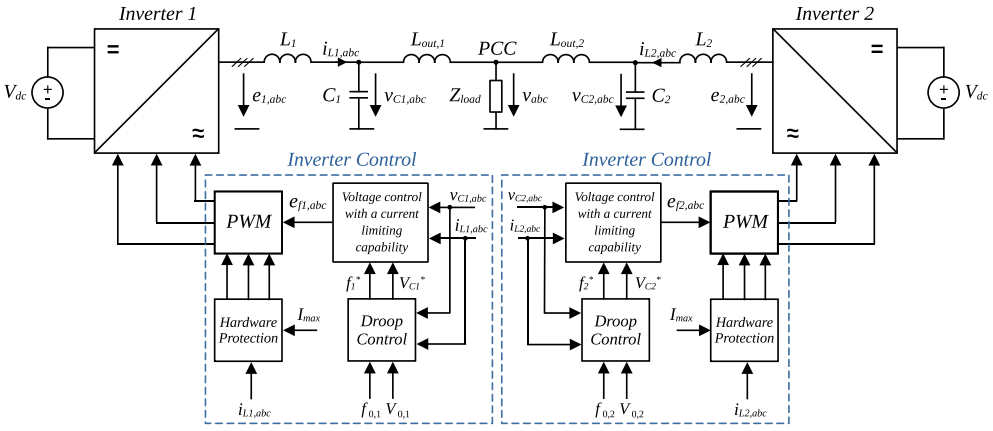

Fig. 1. Overall schematic diagram of two high-power three-phase inverters connected in parallel forming an inverter-based stand-alone microgrid.

value, which would lead to their destruction [11]. To prevent this, a number of control strategies have been proposed in order to limit the inverter current to its maximum value. These techniques ensure that the inverters remain connected with no risk of damage, while they provide the highest level of current possible in order to trigger the protection systems. Some of these methods include the cascade control with inner current loop [12–15], the transient virtual impedance emulation at the voltage references [16,17], the transition from the voltage source control mode to the current source control mode [18,19], or the dual voltage-current control in which the voltage and current controls always operate in parallel [20].

The majority of these methods limit the current by reducing the voltage amplitude imposed by the inverter, so that the *Q-V* droop and the voltage control remain inactive. By contrast, the *P-f* droop must stay active in order to maintain the system frequency and ensure the synchronization of all the inverters. However, the traditional *P-f* droop does not offer stable performance in current limiting conditions due to the modification of the system response [21].

As a result, the analysis of the synchronization stability of grid-connected inverters in grid-forming mode, in current limiting situations, has recently taken on greater importance [22]. This problem can be studied from the large-signal (transient) synchronization stability of a system, consisting in determining whether or not there are equilibrium points in the operating conditions considered. In [23-25], it is shown that *P-f* droop controlled grid-connected inverters may exhibit transient stability problems for certain voltage dip depths.

In order to extend the stability range, different techniques have been proposed for grid-connected systems. These consist in modifying the frequency control when the current is limited. In [18,26], the study proposes to change to a current source control based on a backup phase-locked loop (PLL), i.e. operation in grid-following mode when an overcurrent is detected. This method does improve operation when the inverters are connected to the main grid in which the synchronous generators guarantee that the frequency is maintained. However, this method cannot be used in inverter-based stand-alone microgrids due to the fact that the inverters would stop regulating the frequency and system stability would not be ensured [27].

To avoid the use of a backup PLL during current limitation, [24] proposes the variable droop control that consists in slowing down the *P-f* droop during the fault by adaptively reducing its slope based on the amplitude of the output voltage. This makes it possible to increase the critical clearing time in order to avoid instability problems at the SC output, irrespective of its duration. However, this method does not resolve the problem of transient stability under current limitation and it is therefore not valid for stand-alone systems in which is necessary to achieve an equilibrium point, for example, in light permanent or harsh transitory overload conditions.

Another control strategy proposed for grid-connected systems is the stability enhanced *P-f* droop control [28,29], which consists in including a term proportional to the q-axis component of the inverter output voltage, v_q, in the conventional *P-f* droop curve. This strategy is based on the fact that, with the current limiting methods employed in [28,29], the inverter stops imposing the phase provided by the frequency droop on the voltage and, therefore, v_q is no longer equal to zero under current limitation, providing information on the phase lag of the inverter in relation to the PCC. Although this technique provides greater transient stability margins in current limitation than the conventional *P-f* droop, it does not prevent instability in situations of deep voltage dips [28]. For this reason, it cannot be used in stand-alone systems due to the fact that it does not guarantee the large-signal stability of the system in severe SC situations.

Due to the fact that one of the causes of the malfunctioning of the *P-f* droop in current limitation is the great influence of voltage on active power, the active current-frequency droop has also been proposed (I_{act}-*f*) [21]. This implementation of the frequency droop offers a similar performance in normal operating conditions and improves the performance of the *P-f* droop during overloads and transient SCs. Despite this, the I_{act}-*f* droop still exhibits stability problems in some operating conditions, as demonstrated in this article.

However, little analysis has been made of the large-signal stability of stand-alone microgrids based on electronic inverters in current limiting situations. This paper will firstly make an analysis of the transient stability synchronization of an inverter-based stand-alone microgrid when the inverters are controlled with the *P-f* and I_{act}-*f* droops in the presence of overloads or SCs at the PCC. To do so, the possible equilibrium points are calculated based on the frequency droop method employed and the phase lag between inverters. This makes it possible to obtain the synchronization limits for the large-signal stability of *P-f* and I_{act}-*f* droops, showing the inability of both methods to guarantee the synchronization of the inverters in the event of any large disturbance.

The use of the conductance-frequency droop (*G-f*) is then proposed, consisting in the implementation of the frequency droop with a variable which we define as the equivalent conductance seen by the inverter, *G*. This variable is calculated as the ratio between the active current exchanged by the inverter and the voltage generated by the same. As will be demonstrated, the *G-f* droop maintains the same performance in normal operating conditions as in overload or SC situations, always guaranteeing the synchronization stability of stand-alone microgrids. Moreover, the *G-f* droop makes it possible to always maintain the maximum voltages and currents at the load, and facilitates the rapid recovery of voltage, with no stability problems, at the end of the overload or SC. A further advantage of the proposed method is that the system dynamics scarcely depend on the operating point in current limitation, in contrast to the response with the *P-f* and I_{act}-*f* droops.

The rest of this paper is organized as follows. Section 2 describes the stand-alone microgrid under study, which comprises two grid-forming

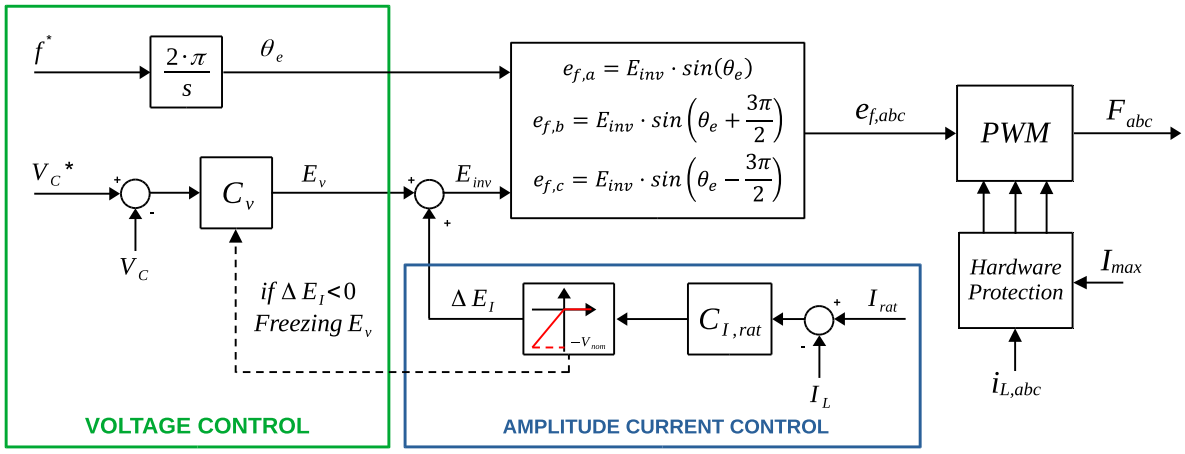

Fig. 2. Blocks diagram of the method selected for the voltage control with a current limiting capability implemented in the high-power inverters of the stand-alone microgrid under study.

inverters, and shows the analysis of the system operation during current limitation. In Section 3, the synchronization transient stability of the case study microgrid is analyzed during current limitation when using the *P-f* and I_{act}-*f* droops. Section 4 presents the proposed *G-f* droop and its performance during current limitation is also analyzed according to operating conditions. Simulation and Hardware-In-the-Loop (HIL) results are shown in Sections 5 and 6, respectively. Finally, conclusions are given in Section 7.

2. System overview

2.1. Description of the stand-alone inverter-based microgrid

The system under study consists in a stand-alone microgrid that is formed by two high-power inverters as shown in Fig. 1. These are connected in parallel at the PCC through their respective LC filters, where L_i is the converter-side inductor and C_i is the filter capacitor, considering the subindex *i* as the number of inverters. The output inductance, $L_{out,i}$, could encompass the transformer leakage inductance, if included, and the line inductance. Given that high-power inverters are under study and assuming short lines in the microgrid, the parasitic resistances of the components can be disregarded so that the output impedances of the inverters are modelled as purely inductive, as shown in Fig. 1. Furthermore, the inverters feed an impedance Z_{load}, which models the set of local loads connected to the system at the PCC. Both inverters present the same local control that calculates the corresponding reference voltages, $e_{fi,abc}$, which are imposed by each converter, by using the inverter frequency setpoint, $f_{0,i}$, the voltage setpoint, $V_{0,i}$, and the measured inductor currents, $i_{Li,abc}$, and output capacitor voltages, $v_{Ci,abc}$. The setpoints $f_{0,i}$ and $V_{0,i}$ of both inverters may be different due to supplementary tasks such as controlling the sharing of the real and reactive powers demanded by the loads.

More specifically, the inverter control is formed by two control loops, the droop control as a superior loop and the voltage control with a current limiting capability as an inferior loop. The droop control calculates the frequency and amplitude references of the voltage, f * and V_C*, through the corresponding setpoints f_0 and V_0 and local measurements. To calculate the reference V_C*, the conventional reactive power-voltage (*Q-V*) droop control is implemented. The method employed for calculating the frequency reference f * is not specified in this subsection, since three different techniques are considered for the frequency droop control in this paper and will be explained in detail in the following subsections.

With regard to the voltage control with a current limiting capability, Fig. 2 shows the method considered in this study. A single voltage control without an inner current control is generally implemented in high-power inverters due to their low switching and sampling frequencies [11]. In this case, the voltage control consists in the open-loop control of the inverter frequency to f * by imposing the phase of the inverter voltages e_{abc}, θ_e, obtained from integrating f *. In relation to the voltage amplitude, a feedback loop is implemented to control the amplitude of the capacitors voltages, V_C, to track V_C* [30,31]. As this technique does not provide the inverter with a current limiting capability, the implementation of an additional control is required. The selected method to limit the current, proposed in [32], consists in including a feedback loop to control the current amplitude, I_L, to the inverter rated current, I_{rat}. This control reduces the voltage amplitude imposed by the inverter, E_{inv}, when $I_L > I_{rat}$ as shown in the block called amplitude current control. As this method is not fast enough to limit the current at the beginning of the overloads or faults, a hardware protection is also included in order to transiently limit the currents when these exceed the selected maximum current by disabling the *PWM* pulses.

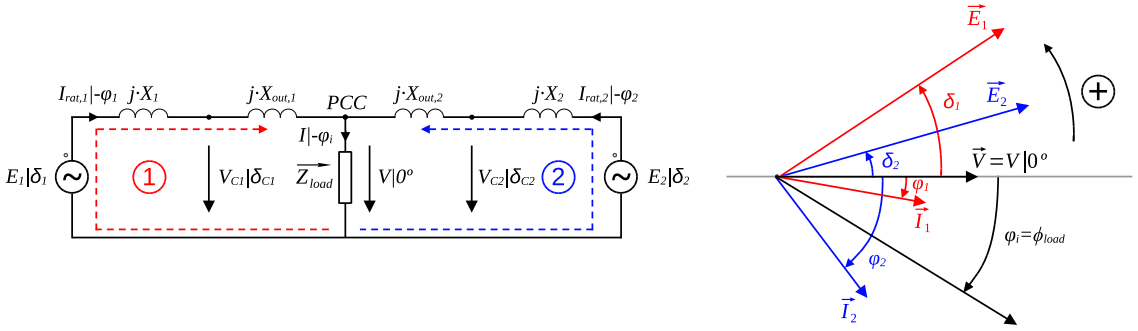

Fig. 3. Phasor model of the stand-alone microgrid during current limitation, including the equivalent circuit for one phase and the phasor diagram.

Further information about the selected strategy to provide the grid-forming inverter with a current limiting capability can be found in [32]. Despite using this specific technique for the current limiting, the subsequent analysis is also applicable for any method that ensures, under current limitation, the generation of the voltage phase determined by the frequency droop control, such as the dual voltage current control [20] or some of the proposals based on the cascaded control [33].

In this way, in normal operation, the inverter is controlled as a voltage source imposing the frequency f * and $V_C = V_C$* as $I_L < I_{rat}$. Whereas in the presence of overloads or short-circuits, i.e. during current limitation, the control still imposes f * but V_C is reduced below V_C* to guarantee that $I_L = I_{rat}$. As a result, the inverter frequency and thus the inverter phase are always dictated by the frequency droop control.

2.2. Analysis of the microgrid operation during current limitation

Figure 3 shows the phasor model of the stand-alone microgrid shown in Fig. 1 with both inverters operating under current limitation, including the equivalent circuit and phasor diagram considering $\overrightarrow{V}$ as the phase angle reference. In this way, the phase angles of the inverters voltages, δ_1 and δ_2, correspond to the inverters power angles. This model has been considered to study the synchronization stability of the system during current limitation, which strongly depends on the frequency droop control employed. Perfect reference tracking is assumed for the voltage and current controls. As a result, it can be considered that $I_{L,1} = I_{rat.1}$ and $I_{L,2} = I_{rat,2}$ during current limitation.

The circuit under study is formed by two meshes, defined as 1 and 2 in Fig. 3, that are connected through the load impedance, which can be defined as

$$\overrightarrow{Z_{load}} = R_{load} + j \cdot X_{load} = Z_{load}|\phi_{load}. \tag{1}$$

Applying Kirchoff's voltage law to meshes 1 and 2 of the equivalent circuit, the following two equations are obtained:

$$\overrightarrow{E_1} = j\cdot\left(X_1 + X_{out,1}\right)\cdot\overrightarrow{I_1} + \overrightarrow{Z_{load}}\cdot\left(\overrightarrow{I_1} + \overrightarrow{I_2}\right), \tag{2}$$

$$\overrightarrow{E_2} = j\cdot\left(X_2 + X_{out,2}\right)\cdot\overrightarrow{I_2} + \overrightarrow{Z_{load}}\cdot\left(\overrightarrow{I_1} + \overrightarrow{I_2}\right). \tag{3}$$

From the phasor diagram in Fig. 3, the phasor of the total current fed to the load, $\overrightarrow{I}$, is defined as

$$\overrightarrow{I} = \overrightarrow{I_1} + \overrightarrow{I_2} = I|-\phi_{load} \tag{4}$$

Considering the case that $I_{rat,1} = I_{rat,2} = I_{rat}$, the current $\overrightarrow{I}$ in (4) can be expressed as

$$\overrightarrow{I} = 2\cdot I_{rat}\cdot cos\left(\frac{\varphi_1 - \varphi_2}{2}\right)\Big| - \frac{\varphi_1 + \varphi_2}{2}. \tag{5}$$

From (4) and (5), the phase angle φ_2 can be expressed as a function of φ_1 as

$$\varphi_2 = 2\cdot\phi_{load} - \varphi_1\ . \tag{6}$$

Then, substituting (5) and (6) into the mesh equations (2) and (3) gives the following set of four equations:

$$E_1\cdot\cos(\delta_1) = \left(X_1 + X_{out,1}\right)\cdot I_{rat}\cdot\sin(\varphi_1) + 2\cdot Z_{load}\cdot I_{rat}\cdot\cos(\varphi_1 - \phi_{load}) \tag{7}$$

$$E_1\cdot\sin(\delta_1) = \left(X_1 + X_{out,1}\right)\cdot I_{rat}\cdot\cos(\varphi_1) \tag{8}$$

$$E_2\cdot cos(\delta_2) = \left(X_2 + X_{out,2}\right)\cdot I_{rat}\cdot sin(2\cdot\phi_{load} - \varphi_1) + 2\cdot Z_{load}\cdot I_{rat}\cdot\cos(\varphi_1 - \phi_{load}) \tag{9}$$

$$E_2\cdot\sin(\delta_2) = \left(X_2 + X_{out,2}\right)\cdot I_{rat}\cdot\cos(2\cdot\phi_{load} - \varphi_1). \tag{10}$$

The system operating point during current limitation is defined by solving (7)–(10) as a function of the power angles, δ_1 and δ_2. However, as δ_1 and δ_2 are both referred to the PCC voltage phase, they are not independent and the system actually presents just one independent variable. For this reason, the variable

$$\Delta\delta = \delta_1 - \delta_2 = \theta_{e,1} - \theta_{e,2}\ , \tag{11}$$

which represents the phase difference between the voltages generated by the inverters, is selected as degree of freedom. In this way, by giving values to δ, the values of the variables δ_1, δ_2, E_1, E_2 and φ_1 can be obtained by means of (7)–(11) and, from these, the value of any other variable of the system can be also calculated. For instance, the RMS amplitude of the PCC voltage, V, can be determined using (5) as

$$V = I\cdot Z_{load} = 2\cdot I_{rat}\cdot Z_{load}\cdot\cos(\varphi_1 - \phi_{load})\ . \tag{12}$$

In the following, the system variables are expressed in per unit values in order to generalize the transient stability analysis to inverter-based stand-alone microgrids of any power capacity level. Considering the rated power of one inverter, S_{rat}, as the base power and the rated voltage, V_{rat}, as the base voltage, the per unit voltage v during current limitation can be obtained from (12) as

$$v = \frac{2}{y_{load}}\cdot cos(\varphi_1 - \phi_{load}), \tag{13}$$

where $y_{load} = 1/z_{load}$ is the per unit load admittance.

In contrast to normal operating conditions where the PCC voltage v remains practically equal to the rated voltage regardless of $\Delta\delta$, during current limitation, the voltage v varies with the load parameters y_{load} and ϕ_{load} and also with the phase angle φ_1 that in turn depends on $\Delta\delta$. According to (6) and (13), the maximum feasible voltage $v_{max} = 2/y_{load}$ is achieved when $\varphi_1 = \varphi_2 = \phi_{load}$ meaning that the currents $\overrightarrow{I_1}$, $\overrightarrow{I_2}$ and $\overrightarrow{I}$ are in phase and the inverters do not exchange current. Fig. 4 depicts the voltage v as a function of $\Delta\delta$ during current limitation for a case study overload with $\phi_{load} = 5°$ and $y_{load} = 2.5$, equivalent to a 25 % overload as the rated load admittance of the case study microgrid formed by two inverters is $y_{load,rat} = 2$. The output impedances of the inverters have been considered equal, i.e. $X_1 + X_{out,1} = X_2 + X_{out,2}$, in order to facilitate the exposition.

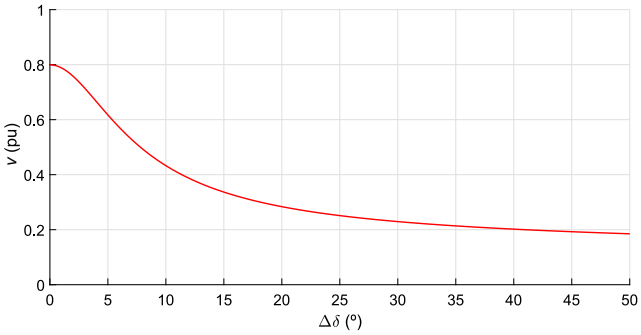

Fig 4. v-$\Delta\delta$ curves during current limitation with $y_{load} = 2.5$ and $\phi_{load} = 5°$.

As can be observed, the maximum voltage corresponds to the theoretical maximum $v_{max} = 2/y_{load}$. In this case, since $X_1 + X_{out,1} = X_2 + X_{out,2}$, this point happens when the inverter voltages are completely in phase, $\Delta\delta = 0$. As $\Delta\delta$ increases, the difference of the current phase angles, φ_1–φ_2, also increases, causing the inverters to start to exchange current. As a result, the current fed to the load decreases, leading to a reduction in the voltage. Therefore, in order to provide the load with a current that is as high as possible, thereby ensuring a voltage close to v_{max} at the PCC during current limitation, the frequency droop control should maintain the inverters synchronized with a low $\Delta\delta$. This is important in order to reliably operate the microgrid, which requires maintaining the voltage v within the limits required by the codes during light permanent overloads and providing a high level of current in the presence of short-circuits in order to help trigger the opening of the

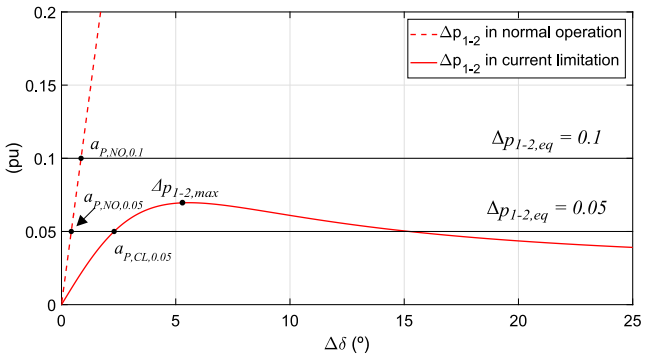

Fig. 5. $\Delta p_{1\text{-}2}$-$\Delta\delta$ curves in normal operating conditions and during current limitation with $y_{load} = 2.5$ and $\phi_{load} = 5°$ including the equilibrium points with *P-f* droop for $\Delta p_{1\text{-}2,eq} = 0.05$ and $\Delta p_{1\text{-}2,eq} = 0.1$.

protection systems. During current limitation, the phase displacement between inverters considerably depends on the method employed for the frequency droop control.

3. Transient stability analysis during current limitation

3.1. Analysis with P-f droop

The analysis of the synchronization transient stability is carried out by assessing, under different operating conditions, whether or not a stable equilibrium point exists. A necessary condition to reach this equilibrium point is that all the inverters in the microgrid must be synchronized. This means that they all generate exactly the same frequency in steady-state operation. In this way, the transient stability depends on the method employed for the frequency droop control.

Assuming that the two grid-forming inverters of the case-study microgrid regulate frequency with the conventional *P-f* droop and the same droop gain, M_f, the inverter frequency is dictated according to the following relationship:

$$f_i^* = f_{0,i} - M_f \cdot p_{e,i} \; with \; i = 1,2 \tag{14}$$

where $p_{e,i}$ is the estimated active power of each inverter in per unit value.

Considering the per unit offset errors, $p_{offset,i}$, that are generally introduced in the local estimation of the active power, the power $p_{e,i}$ can be expressed as

$$p_{e,i} = p_i + p_{offset,i} \; with \; i = 1,2, \tag{15}$$

where p_i is the per unit active power of each inverter.

The equilibrium point will be reached once $f_1{}^* = f_2{}^*$. Replacing (14) and (15), this condition results in

$$f_{0,1} - M_f \cdot (p_1 - p_{offset,1}) = f_{0,2} - M_f \cdot (p_2 - p_{offset,2}). \tag{16}$$

According to this, in order to reach the equilibrium point, the system has to be capable of achieving a difference of $\Delta p_{1\text{-}2} = p_1 - p_2$ equal to

$$\Delta p_{1-2,eq} = \frac{f_{0,1} - f_{0,2}}{M_f} + (p_{offset,1} - p_{offset,2}), \tag{17}$$

where $\Delta p_{1\text{-}2,eq}$ is the per unit active power difference required by the *P-f* droop at the equilibrium point.

As can be observed, $\Delta p_{1\text{-}2,eq}$ depends on the difference between the frequency setpoints. In fact, the frequencies $f_{0,1}$ and $f_{0,2}$ are modified in normal operation to carry out tasks such as managing the energy of the stand-alone system [34,35], or secondary regulation [36]. Moreover, even if $f_{0,1} = f_{0,2}$, the offset errors in the estimated active power lead to $\Delta p_{1\text{-}2,eq} \neq 0$. Thus, the active power difference between inverters, $\Delta p_{1\text{-}2}$, must always offer the capability of increasing up to $\Delta p_{1\text{-}2,eq}$ so that the equilibrium point can be achieved.

Given the equivalent circuit in Fig. 3, the active power provided by each inverter, P_i, can be expressed as

$$P_i = \frac{3 \cdot E_i \cdot V}{X_i + X_{out,i}} \cdot \sin(\delta_i) \; with \; i = 1,2. \tag{18}$$

Thus, the active power difference between both inverters can be calculated as

$$\Delta P_{1-2} = P_1 - P_2 = 3 \cdot V \cdot \left(\frac{E_1}{X_1 + X_{out,1}} \cdot \sin(\delta_1) - \frac{E_2}{X_2 + X_{out,2}} \cdot \sin(\delta_2) \right). \tag{19}$$

Based on (19), Fig. 5 shows the $\Delta p_{1\text{-}2}$-$\Delta\delta$ curves for normal operation and during current limitation for the case study overload. If there were no current limitation, i.e. in normal operation, as the voltages E_i and V remain practically unchanged, $\Delta p_{1\text{-}2}$ quickly increases with $\Delta\delta$. As a result, a high difference $\Delta p_{1\text{-}2}$ can be obtained with low $\Delta\delta$ as shown in Fig. 5. In the figure, the points $a_{P,NO,0.05}$ and $a_{P,NO,0.1}$ represent the equilibrium points in normal operation for $\Delta p_{1\text{-}2,eq} = 0.05$ and $\Delta p_{1\text{-}2,eq} = 0.1$, respectively, achieved since $\Delta p_{1\text{-}2} = \Delta p_{1\text{-}2,eq}$. As can be observed, for $\Delta p_{1\text{-}2,eq} = 0.05$, the phase difference between inverters at the equilibrium point is $\Delta\delta_{P,NO,0.05} = 0.45°$, while for $\Delta p_{1\text{-}2,eq} = 0.1$, the equilibrium point is reached with $\Delta\delta_{P,NO,0.1} = 0.91°$. Thus, the *P-f* droop presents a transiently stable response in normal operation maintaining the inverters synchronized with a low $\Delta\delta$ independently of the value of $\Delta p_{1\text{-}2,eq}$.

However, this method does not offer such a satisfactory performance during current limitation. In this situation, the voltages E_1, E_2 and V decrease with $\Delta\delta$ to maintain $I_{L,1} = I_{L,2} = I_{rat}$ resulting in the modification of the $\Delta p_{1\text{-}2}$-$\Delta\delta$ curve. As shown in Fig. 5, this causes $\Delta p_{1\text{-}2}$ to slowly increase for low $\Delta\delta$ and in fact $\Delta p_{1\text{-}2}$ can either increase or decrease with $\Delta\delta$. There is thus a maximum achievable active power difference, $\Delta p_{1\text{-}2,\max}$, that can be reached when the inverters are in these conditions. As a result, depending on the value of $\Delta p_{1\text{-}2,\max}$ and $\Delta p_{1\text{-}2,eq}$, the *P-f* droop presents two different performances during current limitation:

i. $\Delta p_{1\text{-}2,eq} < \Delta p_{1\text{-}2,\max}$: an equilibrium point $a_{P,CL,0.05}$ exists for $\Delta p_{1\text{-}2,eq} = 0.05$, as shown in Fig. 5, meaning that the system is transiently stable with *P–f* droop during current limitation. Nevertheless, the phase difference between inverters at $a_{P,CL,0.05}$ is $\Delta\delta_{P,CL,0.05} = 2.53°$, almost six times higher than $\Delta\delta_{P,NO,0.05}$ causing a higher decrease of the PCC voltage v (see Fig. 4).
ii. $\Delta p_{1\text{-}2,eq} > \Delta p_{1\text{-}2,\max}$: As can be observed in Fig. 5, there is no equilibrium point during current limitation for $\Delta p_{1\text{-}2,eq} = 0.1$, therefore the system with *P–f* droop in this scenario is transiently unstable leading to the desynchronization of the inverters.

In this way, the stability boundaries of the *P-f* droop during current limitation are defined by the maximum achievable difference $\Delta p_{1\text{-}2,\max}$. In order to calculate $\Delta P_{1\text{-}2,\max}$, equations (8), (10) and (12) are firstly substituted into (19) leading to express the active power difference $\Delta P_{1\text{-}2}$ as

$$\Delta P_{1-2} = 3 \cdot Z_{load} \cdot I_{rat}^2 \cdot [\cos(2 \cdot \varphi_1 - \phi_{load}) - \cos(2 \cdot \varphi_1 - 3 \cdot \phi_{load})]. \tag{20}$$

Then, the derivative of (20) in relation to φ_1 is imposed to be equal to zero leading to the following two solutions:

$$\begin{aligned} Solution \;\; 1: \; \varphi_{1,\Delta P_{max}} &= \phi_{load} + 45^\circ, \;\; \varphi_{2,\Delta P_{max}} = \phi_{load} - 45^\circ, \\ Solution \;\; 2: \; \varphi_{1,\Delta P_{max}} &= \phi_{load} - 45^\circ, \;\; \varphi_{2,\Delta P_{max}} = \phi_{load} + 45^\circ, \end{aligned} \tag{21}$$

where $\varphi_{1,\Delta Pmax}$ and $\varphi_{2,\Delta Pmax}$ are the phase angles of the currents $\vec{I_1}$ and $\vec{I_2}$ for which the maximum active power difference, $\Delta P_{1\text{-}2,\max}$, is reached.

Substituting (21) into (20), the maximum achievable active power difference is calculated as

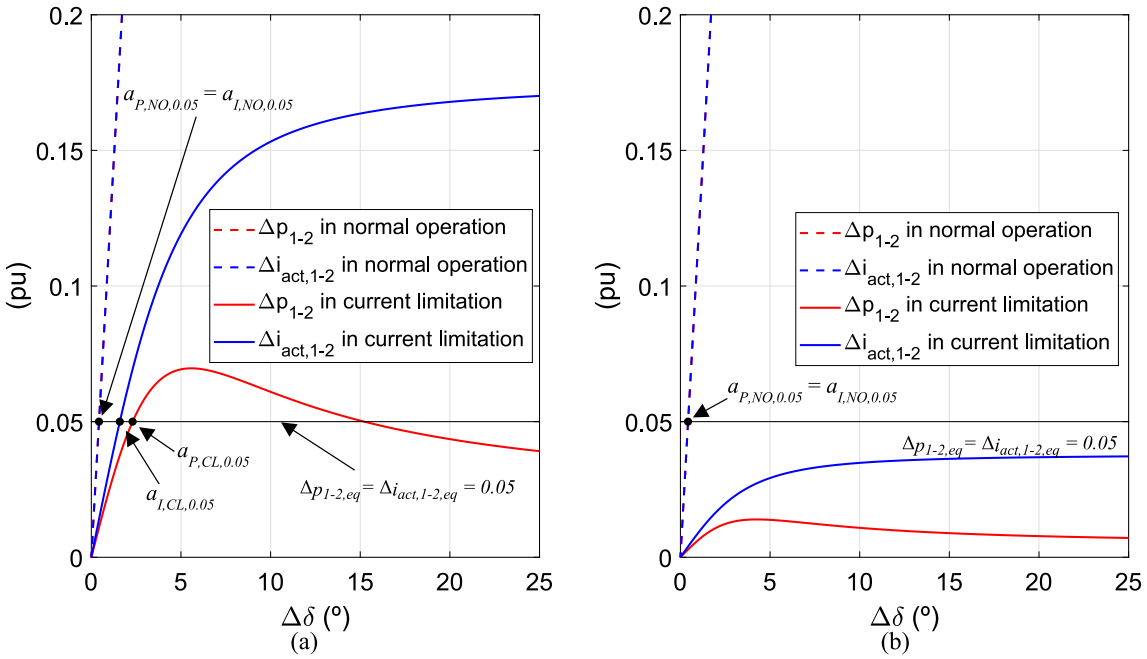

Fig. 6. $\Delta p_{1\text{-}2}$-$\Delta\delta$ and $\Delta i_{act,1\text{-}2}$-$\Delta\delta$ curves in normal operating conditions and during current limitation with $y_{load} = 2.5$ including the equilibrium points with *P-f* and I_{act}-*f* droops for $\Delta p_{1\text{-}2,eq} = \Delta i_{act,1\text{-}2,eq} = 0.05$ in two different cases: a) With $\phi_{load} = 5°$. (b) With $\phi_{load} = 1°$.

$$\Delta P_{1-2,max} = \pm 6 \cdot Z_{load} \cdot I_{rat}^2 \cdot sin(\phi_{load}) \tag{22}$$

From (22), the maximum difference $\Delta P_{1\text{-}2,\max}$ can be expressed in per unit value as

$$\Delta p_{1-2,max} = \pm \frac{2}{y_{load}} \cdot sin(\phi_{load}). \tag{23}$$

According to (23), the maximum achievable active power difference between inverters during current limitation, which determines the transient stability boundary when using the *P-f* droop, depends on both the magnitude and power factor of the load impedances seen by the inverters, y_{load} and ϕ_{load}. In particular, in the event of a pure resistive overload or short-circuit, the maximum achievable difference $\Delta p_{1\text{-}2,\max}$ will be equal to zero according to (23) causing any offset error in the estimation of p_i to lead to $\Delta p_{1\text{-}2,eq} \neq 0$ and to provoke the transient instability of the system regardless of y_{load}. Thus, the *P-f* droop cannot guarantee the transient stability of the inverters for all possible operating conditions.

3.2. Analysis with I_{act}–*f* droop

The transient stability margins of the stand-alone microgrid can be enhanced by using the I_{act}–*f* droop. Assuming that the two grid-forming inverters of the casestudy microgrid regulate the frequency with the I_{act}–*f* droop and the same M_f, the inverter frequency is dictated according to the following relationship:

$$f_i^* = f_{0,i} - M_f \cdot i_{act,e,i} \; with \; i = 1, 2, \tag{24}$$

where $i_{act,e,i}$ is the estimated active current of each inverter in per unit value.

In order to model the per unit offset error, $i_{act,offset,i}$, introduced in the estimation of the active current, the current $i_{act,e,i}$ can be defined as

$$i_{act,e,i} = i_{act,i} + i_{act,offset,i} \; with \; i = 1, 2, \tag{25}$$

where $i_{act,i}$ is the per unit active current of each inverter.

Based on the condition that $f_1^* = f_2^*$ at the equilibrium point, the substitution of (24) and (25) results in

$$\Delta i_{act,1-2,eq} = \frac{f_{0,1} - f_{0,2}}{M_f} + (i_{act,offset,1} - i_{act,offset,2}), \tag{26}$$

where $\Delta i_{act,1\text{-}2,eq}$ is the per unit active current difference required by the I_{act}-*f* droop at the equilibrium point.

In comparison with (17), both the *P-f* and I_{act}-*f* droops require a similar per unit difference at the equilibrium point according to the reference frequencies and per unit offset errors. Thus, in the same way, the real active current difference between inverters, $\Delta i_{act,1\text{-}2}$, must always offer the capability of increasing up to $\Delta i_{act,1\text{-}2,eq}$ so that the equilibrium point can be reached.

The active current provided by each inverter, $I_{act,i}$, can be locally calculated as

$$I_{act,i} = \frac{P_i}{3 \cdot V_{Ci}} with \; i = 1, 2. \tag{27}$$

According to Fig. 3, the active power exchanged by each inverter, P_i, can be also expressed as

$$P_i = \frac{3 \cdot E_i \cdot V_{Ci}}{X_i} \cdot sin(\delta_{inv,i}) \; with \; i = 1, 2, \tag{28}$$

where $\delta_{inv,i} = \delta_i - \delta_{Ci}$ is the inverter power angle, representing the phase difference between the voltage generated by each inverter, $\overrightarrow{E_i}$, and the voltage at the output capacitors of each inverter, $\overrightarrow{V_{Ci}}$.

In this manner, substituting (28) into (27), the active current can be expressed as

$$I_{act,i} = \frac{E_i}{X_i} \cdot \sin(\delta_{inv,i}) \; with \; i = 1, 2. \tag{29}$$

Thereby, the difference in the active current between both inverters, $\Delta I_{act,1\text{-}2}$, can be calculated as

$$\Delta I_{act,1-2} = \frac{E_1}{X_1} \cdot \sin(\delta_{inv,1}) - \frac{E_2}{X_2} \cdot \sin(\delta_{inv,2}). \tag{30}$$

In comparison with (19), the main difference between $\Delta P_{1\text{-}2}$ and $\Delta I_{act,1\text{-}2}$ is that the latter presents a lower influence of the voltage at the PCC.

Based on (30), Fig. 6 shows the $\Delta p_{1\text{-}2}$-$\Delta\delta$ and $\Delta i_{act,1\text{-}2}$-$\Delta\delta$ curves for normal operation and during current limitation for an overload of $y_{load} = 2.5$ with two different power factors: (a) $\phi_{load} = 5^{\circ}$, (b) $\phi_{load} = 1^{\circ}$. In normal operation, the $\Delta p_{1\text{-}2}$-$\Delta\delta$ and $\Delta i_{act,1\text{-}2}$-$\Delta\delta$ curves are equal and thus the I_{act}-f droop provides the same stable performance as the P-f droop. In fact, considering that $\Delta p_{1\text{-}2,eq} = \Delta i_{act,1\text{-}2,eq} = 0.05$, the equilibrium point with I_{act}-f droop in normal operation, $a_{I,NO,0.05}$, shows the same phase difference between inverters as the equilibrium point with P-f droop as shown in Fig. 6. As a result, the I_{act}-f droop also maintains the inverters synchronized with a low $\Delta\delta$ irrespective of $\Delta i_{act,1\text{-}2,eq}$ in normal operation.

By contrast, during current limitation, the $\Delta p_{1\text{-}2}$–$\Delta\delta$ and $\Delta i_{act,1\text{-}2}$–$\Delta\delta$ curves present a different trend. The difference $\Delta i_{act,1\text{-}2}$ always increases with $\Delta\delta$ due to its lower dependence on the voltage v leading to $\Delta i_{act,1\text{-}2} > \Delta p_{1\text{-}2}$ for any value of $\Delta\delta$. Despite this, the slope of the $\Delta i_{act,1\text{-}2}$-$\Delta\delta$ curve decreases with $\Delta\delta$ resulting in a maximum difference $\Delta i_{act,1\text{-}2,\max}$ that can be reached. Consequently, the I_{act}-f droop also presents two different performances depending on the value of $\Delta i_{act,1\text{-}2,\max}$ in relation to $\Delta i_{act,1\text{-}2,eq}$.

i. $\underline{\Delta i_{act,1\text{-}2,eq} < \Delta i_{act,1\text{-}2,\max}}$: As shown in Fig. 6(a) with $\phi_{load} = 5^{\circ}$, an equilibrium point exists during current limitation for $\Delta i_{act,1\text{-}2,eq} = 0.05$, $a_{I,CL,0.05}$, meaning that the I_{act}-f droop maintains the transient stability of the system in this case. As can be observed, the phase difference between inverters at $a_{I,CL,0.05}$ is $\Delta\delta_{I,CL,0.05} = 1.57^{\circ}$, considerably lower than $\Delta\delta_{P,CL,0.05} = 2.53^{\circ}$. Thanks to this, a higher voltage is ensured at the PCC during current limitation (see Fig. 4) with I_{act}-f droop, thus offering better performance than the P-f droop. However, the I_{act}-f droop also gives a lower response than in normal operation as $\Delta\delta_{I,CL,0.05} > \Delta\delta_{I,NO,0.05}$.

ii. $\underline{\Delta i_{act,1\text{-}2,eq} > \Delta i_{act,1\text{-}2,\max}}$: As shown in Fig. 6(b) with $\phi_{load} = 1^{\circ}$, in this situation there are no equilibrium points with either the P-f droop or the I_{act}-f droop for $\Delta p_{1\text{-}2,eq} = \Delta i_{act,1\text{-}2,eq} = 0.05$ during current limitation. As a result, the system will become transiently unstable with the I_{act}-f droop in this case leading to the desynchronization of the inverters.

In a similar way to the P-f droop, the stability boundaries with the I_{act}-f droop during current limitation are defined by the maximum achievable difference $\Delta i_{act,1\text{-}2,\max}$. In order to facilitate the calculation of an approximate $\Delta I_{act,1\text{-}2,\max}$, the active current of each inverter is determined as

$$I_{act,i} = \frac{P_i}{3 \cdot V} \; with \; i = 1,\ 2. \tag{31}$$

In this way, substituting (18) into (31), the difference $\Delta I_{act,1\text{-}2}$ can be calculated as

$$\Delta I_{act,1-2} = \frac{P_1 - P_2}{V} = \frac{E_1}{X_1 + X_{out,1}} \cdot \sin(\delta_1) - \frac{E_2}{X_2 + X_{out,2}} \cdot \sin(\delta_2). \tag{32}$$

Substituting (8) and (10) into (32), the difference $\Delta I_{act,1\text{-}2}$ during current limitation can be also expressed as

$$\Delta I_{act,1-2} = I_{rat} \cdot [\cos(\varphi_1) - \cos(2 \cdot \phi_{load} - \varphi_1)] \tag{33}$$

Thus, the derivative of (33) in relation to φ_1 is imposed to be equal to zero leading to the following two solutions

$$\begin{aligned} &Solution\ 1: \ \varphi_{1,\Delta I_{act,max}} = \phi_{load} + 90^{\circ}, \ \varphi_{2,\Delta I_{act,max}} = \phi_{load} - 90^{\circ} \\ &Solution\ 2: \ \varphi_{1,\Delta I_{act,max}} = \phi_{load} - 90^{\circ}, \ \varphi_{2,\Delta I_{act,max}} = \phi_{load} + 90^{\circ} \end{aligned} \tag{34}$$

where $\varphi_{1,\Delta I_{act,max}}$ and $\varphi_{2,\Delta I_{act,max}}$ are the two phase angles of the current $\overrightarrow{I_1}$ and $\overrightarrow{I_2}$ for which the maximum active current difference, $\Delta i_{act,1\text{-}2,\max}$, occurs.

As a result, $\Delta i_{act,1\text{-}2,\max}$ is achieved when $|\varphi_1 - \varphi_2| = 180^{\circ}$ resulting in $I = 0$ and thus $V = 0$ according to (5) and (12), so this is not a desired operating point. Substituting (34) into (33), the maximum active current difference is calculated as

$$\Delta I_{act,1-2,max} = \pm 2 \cdot I_{rat} \cdot \sin(\phi_{load}). \tag{35}$$

From (35), the maximum difference $\Delta I_{act,1\text{-}2,\max}$ can be expressed in per unit value as

$$\Delta i_{act,1-2,max} = \pm 2 \cdot \sin(\phi_{load}). \tag{36}$$

In comparison with (23), $\Delta i_{act,1\text{-}2,\max}$ is not influenced by the overload level, y_{load}, leading to $|\Delta i_{act,1\text{-}2,max}| > |\Delta p_{1\text{-}2,max}|$ for any overload or short-circuit with $\phi_{load} \neq 0$. Thus, the I_{act}-f droop provides a wider range of synchronization large-signal stability than the P-f droop, i.e. $\Delta i_{act,1\text{-}2,\max} > \Delta p_{1\text{-}2,\max}$, whenever $\phi_{load} > 0^{\circ}$. However, in the event of a pure resistive disturbance, the maximum achievable difference $\Delta i_{act,1\text{-}2,\max}$ will also be close to zero causing any offset error in the estimation of $i_{act,i}$ to entail the synchronization transient instability of the system such as when using the P-f droop. Thus, neither is it possible for the I_{act}-f droop to guarantee the transient stability of the system for all possible operating conditions.

4. Proposed frequency droop control, G-f droop

As demonstrated in the section above, the P-f and I_{act}-f droops cannot guarantee that the microgrid inverters will remain synchronized regardless of the operating conditions since the variables P and I_{act} depend highly on the system voltages. To avoid this, in this article, it is proposed to implement the frequency droop control by using the variable G_i that can be locally calculated as

$$G_i = \frac{I_{act,i}}{E_i} = \frac{P_i}{3 \cdot E_i \cdot V_{Ci}} \; with \; i = 1,2. \tag{37}$$

The division of the exchanged active power P_i (unit W) by the product of the voltages $E_i \cdot V_{C,i}$ (unit V^2) leads to the unit Ω^{-1} that is the standard unit of conductance. Therefore, the control variable G_i can be defined as the equivalent conductance seen by each inverter. In this way, the sum of the equivalent conductances of all inverters connected in parallel is equal to the total conductance of the load impedances connected at the microgrid. It is worth noting that the calculation of the conductance G_i does not imply the introduction of additional sensors, since the amplitudes E_i and $V_{C,i}$ are already determined at the inverter to carry out the voltage control and other tasks.

Substituting (28) into (37), the equivalent conductance can also be expressed as

$$G_i = \frac{1}{X_i} \cdot \sin(\delta_{inv,i}) \; with \; i = 1,2. \tag{38}$$

Therefore, G_i only changes with the power angle of the inverter, $\delta_{inv,i}$, constantly providing reliable information with regard to the phase displacement between the inverter voltage, $\overrightarrow{E_i}$, and the capacitor voltage, $\overrightarrow{V_{C,i}}$.

Based on the equivalent conductance G_i, the G-f droop is proposed in this article to maintain the inverters synchronized under all possible operating conditions. Similarly to the P-f and I_{act}-f droops, this method dictates the inverter frequency according to the following relationship:

$$f_i^* = f_{0,i} - M_f \cdot g_{e,i} \; with \; i = 1,2, \tag{39}$$

where $g_{e,i}$ is the per unit estimated equivalent conductance seen by each inverter that is calculated as

$$g_{e,i} = \frac{G_{e,i}}{G_{rat}} = G_{e,i} \cdot \frac{3 \cdot V_{rat}^2}{S_{rat}}, \tag{40}$$

where G_{rat} is the rated conductance of one inverter.

In order to model the per unit offset errors, $g_{offset,i}$, introduced in the

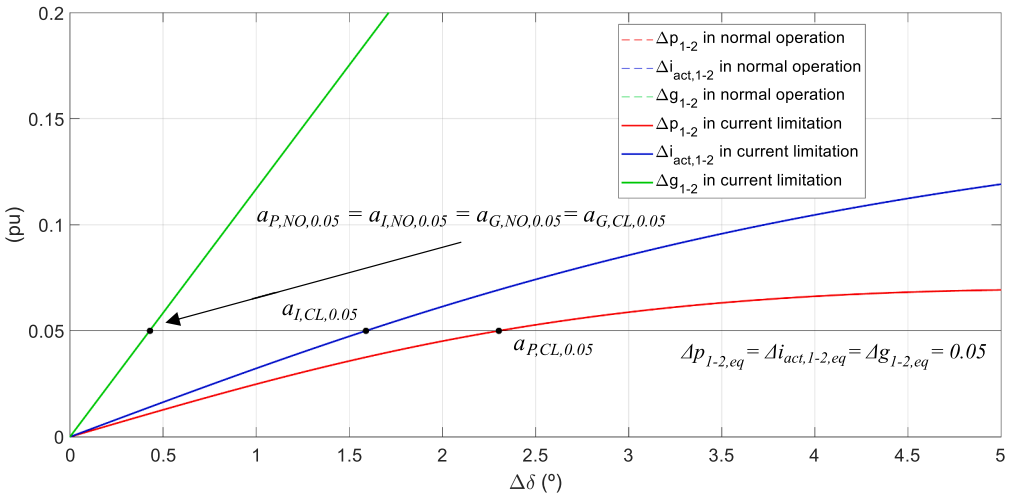

Fig. 7. $\Delta p_{1\text{-}2}$-$\Delta\delta$, $\Delta i_{act,1\text{-}2}$-$\Delta\delta$ *and* $\Delta g_{1\text{-}2}$-$\Delta\delta$ curves in normal operating conditions and during current limitation with $y_{load} = 2.5$ and $\phi_{load} = 5°$ including the equilibrium points with *P-f*, I_{act}-*f* and *G-f* droops for $\Delta p_{1\text{-}2,eq} = \Delta i_{act,1\text{-}2,eq} = \Delta g_{1\text{-}2,eq} = 0.05$.

estimation of the equivalent conductance, the conductance $g_{e,i}$ can be expressed as

$$g_{e,i} = g_i + g_{offset,i} \; with \; i = 1, 2, \tag{41}$$

where g_i is the per unit equivalent conductance seen by each inverter.

Substituting (41) into the condition $f_1{}^* = f_2{}^*$, the difference $\Delta g_{1\text{-}2} = g_1 - g_2$ required to achieve the equilibrium point with *G-f* droop, $\Delta g_{1\text{-}2,eq}$, is

$$\Delta g_{1-2,eq} = \frac{f_{0,1} - f_{0,2}}{M_f} + \left(g_{offset,1} - g_{offset,2}\right). \tag{42}$$

Recalling (17) and (26), the *G-f* droop requires a similar per unit difference at the equilibrium point as the *P-f* and I_{act}-*f* droops. Therefore, the real difference of equivalent conductances between inverters, $\Delta g_{1\text{-}2}$, must always offer the capability of increasing up to $\Delta g_{1\text{-}2,eq}$ so that the equilibrium point can be reached.

From (38), the difference of equivalent conductances between both inverters can be defined as

$$\Delta G_{1-2} = \frac{1}{X_1}\cdot\sin\left(\delta_{inv,1}\right) - \frac{1}{X_2}\cdot\sin\left(\delta_{inv,2}\right). \tag{43}$$

The difference of equivalent conductances $\Delta G_{1\text{-}2}$ only varies with the phase difference between inverters without depending on the system voltages E_i and $V_{C,i}$. In this way, the maximum value of the difference $\Delta G_{1\text{-}2}$ scarcely changes with the operating conditions, avoiding the decrease of the maximum reachable difference under current limitation as it happens to the active power and active current (see (23) and (36)). Thanks to this, the proposed *G-f* droop can reach an equilibrium point regardless of the voltage amplitude ensuring always the transient stability of the microgrid and, thus, improving the performance of the *P-f* and I_{act}-*f* droops.

Based on the model presented in Section 2.2, Fig. 7 shows the $\Delta p_{1\text{-}2}$-$\Delta\delta$, $\Delta i_{act,1\text{-}2}$-$\Delta\delta$ and $\Delta g_{1\text{-}2}$-$\Delta\delta$ curves in normal operation and during current limitation for the case study overload. In normal operation, as $E_i \approx V \approx 1$ pu, the $\Delta g_{1\text{-}2}$-$\Delta\delta$ curve is equal to the $\Delta p_{1\text{-}2}$-$\Delta\delta$ and $\Delta i_{act,1\text{-}2}$-$\Delta\delta$ curves. As can be noted, the equilibrium point when using the *G-f* droop for $\Delta g_{1\text{-}2,eq} = 0.05$ in normal operation, $a_{G,NO,0.05}$, exhibits the same phase difference between inverters as the corresponding equilibrium points with *P-f* and I_{act}-*f* droops, $a_{P,NO,0.05}$ and $a_{I,NO,0.05}$. Therefore, the *G-f* droop provides the same stable response in these conditions as the other methods maintaining the inverters synchronized with a low $\Delta\delta$ independently of $\Delta g_{1\text{-}2,eq}$ and ensuring the same accurate sharing of the active power between grid-forming inverters irrespective of the difference between line impedances.

Table 1
Parameters of the microgrid under study – power and control stages.

Symbol	Description	Value
S_{rat}	Inverter Rated Power	1.64 MVA
V_{rat}	Rated Voltage	630 V
I_{rat}	Rated Current	1500 A
V_{dc}	DC-bus voltage	1100 V
f_{rat}	Rated frequency	50 Hz
f_{sw}	Switching frequency	3 kHz
f_s	Sampling frequency	6 kHz
L_1, L_2	Converter-side filter inductor	0.14 pu
C_1, C_2	Filter capacitance	0.03 pu
$L_{out,1}$, $L_{out,2}$	Output inductance	0.01 pu
I_{max}	Maximum current	1.1 pu
M_f	Frequency droop gain	0.5 Hz
M_V	Voltage droop gain	0.12 pu
$f_{c,f}$	Cutoff frequency of $H(s)$	5 Hz

During current limitation, as $\Delta g_{1\text{-}2}$ does not depend on the voltages, the $\Delta g_{1\text{-}2}$-$\Delta\delta$ curve is similar to normal operating conditions always maintaining the same rapid increase of $\Delta g_{1\text{-}2}$ with $\Delta\delta$. Thanks to this, a high difference $\Delta g_{1\text{-}2}$ can also be obtained with low $\Delta\delta$ during current limitation meaning that the equilibrium point with $\Delta g_{1\text{-}2} = \Delta g_{1\text{-}2,eq}$ can always be achieved. As a result, unlike the *P-f* and I_{act}-*f* droops, the inverters controlled with *G-f* droop maintain the transient stability regardless of the value of $f_{0,1}$, $f_{0,2}$, $g_{offset,1}$, $g_{offset,2}$, y_{load} and ϕ_{load}, providing the system with robustness under any operating conditions.

Furthermore, if the *P-f* and I_{act}-*f* droops provide stable performance during current limitation, these methods require a higher phase difference than the *G-f* droop to reach the equilibrium point due to the modification of the $\Delta p_{1\text{-}2}$-$\Delta\delta$ and $\Delta i_{act,1\text{-}2}$-$\Delta\delta$ curve with the operating conditions. For instance, as shown in Fig. 7 for $\Delta p_{1\text{-}2,eq} = \Delta i_{act,1\text{-}2,eq} = \Delta g_{1\text{-}2,eq} = 0.05$ during current limitation, the relationship between the phase differences required by the three methods at the equilibrium point is $\Delta\delta_{P,CL,0.05} > \Delta\delta_{I,CL,0.05} > \Delta\delta_{G,CL,0.05}$ causing the *G-f* droop to ensure the highest voltage at the PCC (see Fig. 4). Moreover, the certainty of maintaining a low $\Delta\delta$ with the *G-f* droop ensures that the highest level of current is delivered to the short-circuit protection system in order to trigger rapid opening.

5. Simulation results

To validate the theoretical analysis of the system performance when using the *P-f* droop, the I_{act}-*f* droop and the proposed *G-f* droop, the inverter-based stand-alone microgrid in Fig. 1 was simulated under

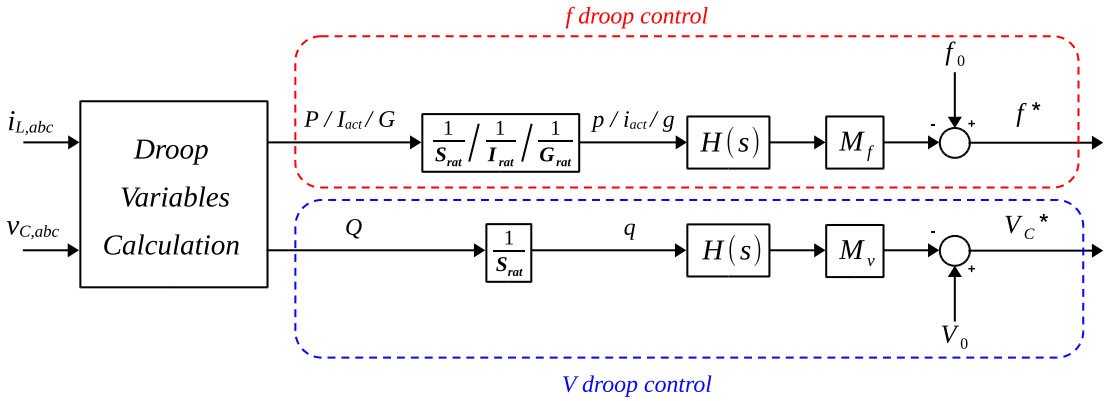

Fig. 8. Blocks diagram of the droop control method $_{implemented}$ in the inverter control.

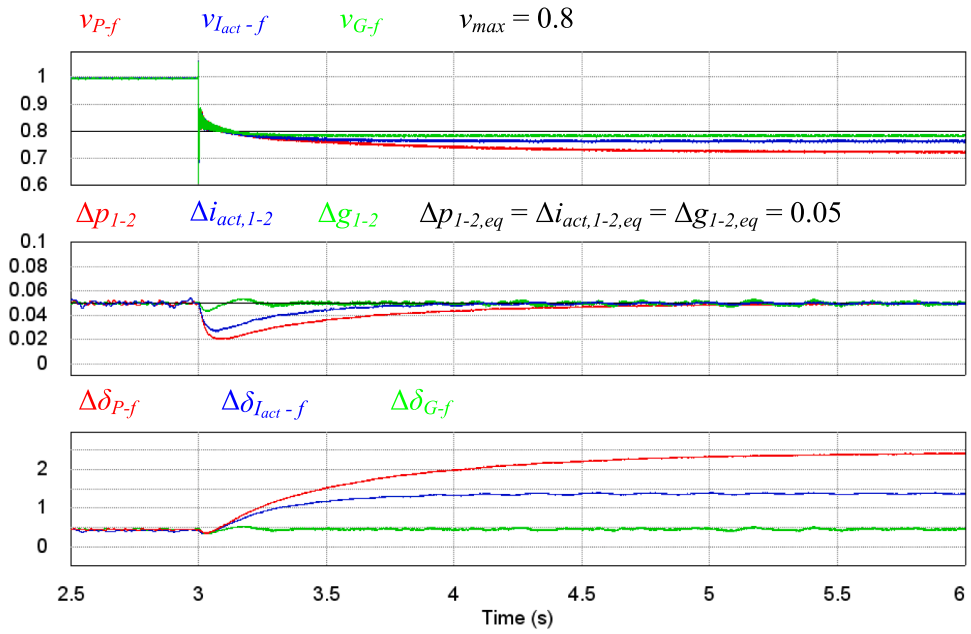

Fig. 9. Simulation waveforms of the inverter-based stand-alone microgrid with *P-f* droop (red), I_{act}*-f* droop (blue) and *G-f* droop (green), requiring $\Delta p_{1\text{-}2,eq} = \Delta i_{act,1\text{-}2,eq} = \Delta g_{1\text{-}2,eq} = 0.05$ in the presence of a 25 % permanent overload, $y_{load} = 2.5$, with $\phi_{load} = 5°$. (For interpretation of the references to colour in this figure legend, the reader is referred to the web version of this article.)

different operating conditions. Table 1 shows the main parameters of the two high-power inverters forming the case study microgrid, including values for both the power and control stages. The same droop gain M_f equal to 0.5 Hz is employed for the three frequency droop controls under study, in such a way that the microgrid frequency will vary between 49.5 and 50.5 Hz in normal operation.

Figure 8 shows the droop control method employed to calculate separately the frequency and voltage references, f^* and V_C^*. The implementation of the three techniques considered for the frequency droop control is depicted including the calculation of the per unit value, a first-order low-pass filter, $H(s)$, and the droop relationship. The voltage droop control is based on the reactive power, Q, and is implemented similarly to the frequency droop control.

Figure 9 shows the simulation waveforms of the stand-alone microgrid with the three frequency droop controls, namely *P-f*, I_{act}*-f* and *G-f* droops. In all cases, $f_{0,1} = f_{0,2}$ is imposed and an estimation offset is included in such a way that $\Delta p_{1\text{-}2,eq} = \Delta i_{act,1\text{-}2,eq} = \Delta g_{1\text{-}2,eq} = 0.05$. At first, the inverters are working in normal operation feeding a load with $y_{load} = 1$ and are controlled as voltage sources causing the voltage at the PCC to remain equal to the rated voltage. In these conditions, the system reaches the same equilibrium point with the three methods, presenting a phase difference $\Delta\delta \approx 0.45°$ and the differences $\Delta p_{1\text{-}2} = \Delta i_{act,1\text{-}2} = \Delta g_{1\text{-}2} = 0.05$ required to reach the equilibrium point.

At second 3, an overload with $\phi_{load} = 5°$ and $y_{load} = 2.5$ (25 % overload) is introduced leading to a transiently stable response in all three cases, as the inverters reach their respective equilibrium points. However, the performance of the system changes depending on the method employed during current limitation. As can be observed, the response with the *P-f* and I_{act}*-f* droops leads to a higher phase difference between inverters at the equilibrium point than in normal operation. This does not occur with the *G-f* droop since the inverters maintain a similar phase difference in both operating conditions, resulting in $\Delta\delta_{P\text{-}f} > \Delta\delta_{I_{act}\text{-}f} > \Delta\delta_{G\text{-}f}$, which is in line with the theoretical results shown in Figure 7 As a result, the *G-f* droop ensures the highest voltage at the PCC, $v_{G\text{-}f} > v_{I_{act}\text{-}f} > v_{P\text{-}f}$, in the presence of the overload. In fact, the voltage $v_{G\text{-}f}$ remains close to the maximum value $v_{max} = 1/y_{load}$, corresponding to $v_{max} = 0.8$ for the overload introduced. Furthermore, as the equivalent conductance g_i scarcely depends on the voltage, the *G-f* droop provides the fastest dynamics following the overload, reaching the equilibrium point in less than 0.3 s and maintaining the same rapidity as in normal

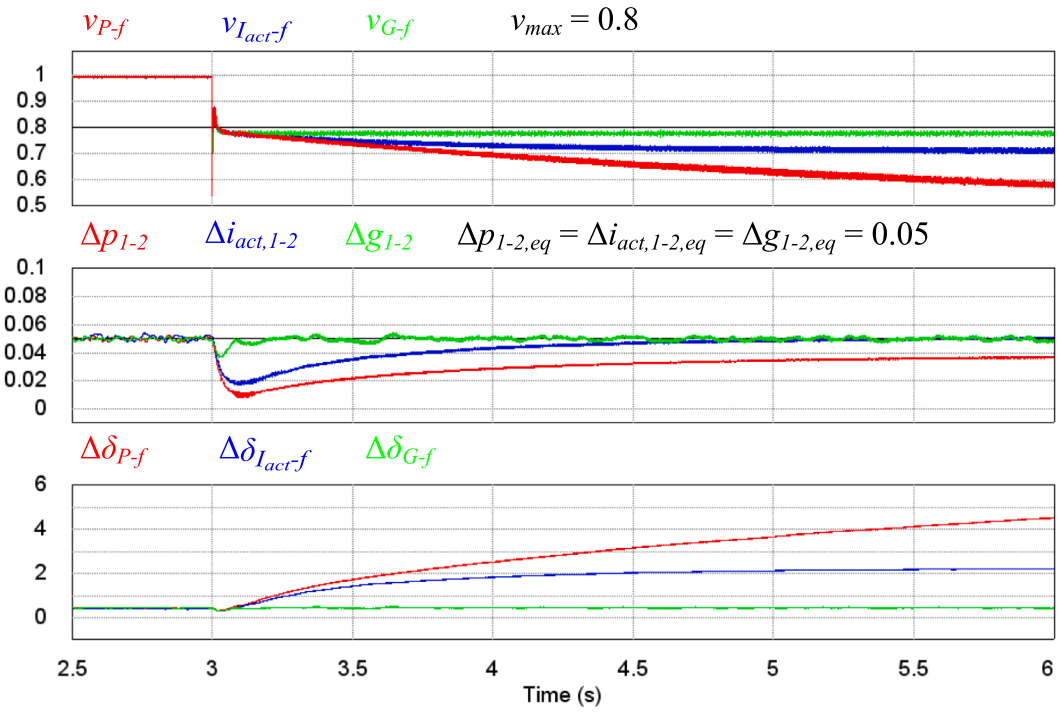

Fig. 10. Simulation waveforms of the inverter_based stand_alone microgrid with *P-f* droop (red), I_{act}*-f* droop (blue) and *G-f* droop (green), requiring $\Delta p_{1\text{-}2,eq} = \Delta i_{act,1\text{-}2,eq} = \Delta g_{1\text{-}2,eq} = 0.05$ in the presence of a 25 % permanent overload, $y_{load} = 2.5$, with $\phi_{load} = 2.5°$. (For interpretation of the references to colour in this figure legend, the reader is referred to the web version of this article.)

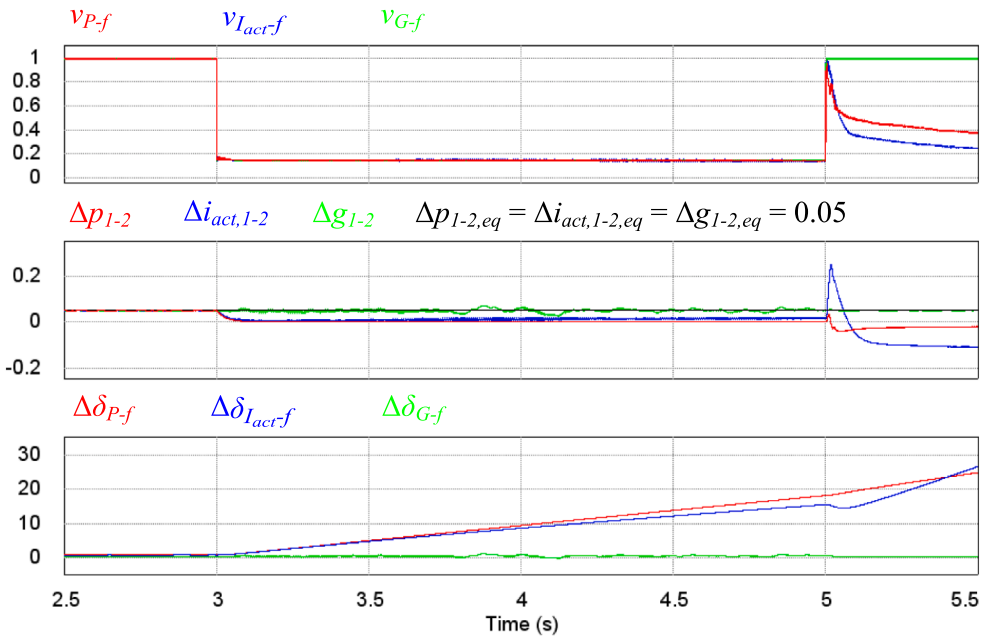

Fig. 11. Simulation waveforms of the inverter-based stand-alone microgrid with *P-f* droop (red), I_{act}*-f* droop (blue) and *G-f* droop (green), requiring $\Delta p_{1\text{-}2,eq} = \Delta i_{act,1\text{-}2,eq} = \Delta g_{1\text{-}2,eq} = 0.05$ in the presence of a resistive symmetrical transient short-circuit with $u_{CC} = 0.15$ and a duration of 2 s (from normal operation to short-circuit and back). (For interpretation of the references to colour in this figure legend, the reader is referred to the web version of this article.)

operation. In contrast, the system dynamics with *P-f* and I_{act}*-f* droops become slower when the overload happens due to the stronger influence of the voltage.

Figure 10 shows the simulation waveforms of the stand-alone microgrid with the three frequency droop controls, when imposing $f_{0,1} = f_{0,2}$ and including an estimation offset that leads to $\Delta p_{1\text{-}2,eq} = \Delta i_{act,1\text{-}2,eq} = \Delta g_{1\text{-}2,eq} = 0.05$. At second 3, an overload with $\phi_{load} = 2.5°$ and $y_{load} = 2.5$ (25 % overload) is introduced. In this case, when using the *P-f* droop an equilibrium point does not exist since $\Delta p_{1\text{-}2,\max} < \Delta p_{1\text{-}2,eq}$, and the system becomes transiently unstable. As a result, the inverters lose the synchronism and the voltage at the PCC drops uncontrollably. As shown in Fig. 10, the maximum difference of active power achieved with $y_{load} = 2.5$ and $\phi_{load} = 2.5°$ is $\Delta p_{1\text{-}2,\max} = 0.037$ matching the theoretical $\Delta p_{1\text{-}2,\max} = 0.035$ calculated according to (23). With regard

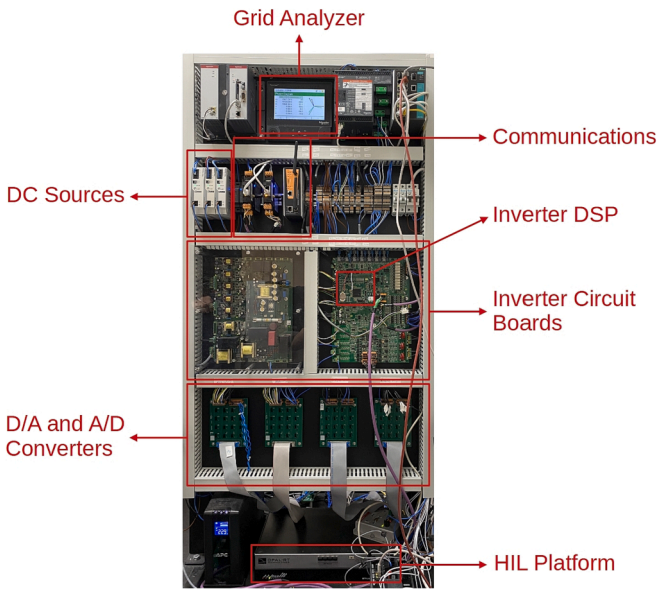

Fig. 12. Hardware-in-the-Loop (HIL) configuration based on OPAL-RT platform.

to the I_{act}-f and G-f droops, the system is transiently stable with both methods, but the second provides the system with a better performance during overload. For $\phi_{load} = 2.5°$, the I_{act}-f droop requires a higher phase difference than for $\phi_{load} = 5°$ to reach the equilibrium point and, thus, the voltage at the PCC decreases to 0.7 pu. Moreover, the I_{act}-f droop becomes slower with the decrease of $v_{I_{act}\text{-}f}$ leading to a higher settling time. Conversely, the G-f droop requires the same phase difference at the equilibrium point for $\phi_{load} = 2.5°$ and $\phi_{load} = 5°$ resulting in the same voltage $v_{G\text{-}f}$ during the overload in both cases. Furthermore, the dynamics of the G-f droop are not affected by ϕ_{load} and the settling time is similar to that obtained in the previous case.

Figure 11 shows the simulation waveforms of the stand-alone microgrid with the three frequency droop controls again imposing $f_{0,1} = f_{0,2}$ and including an estimation offset that leads to $\Delta p_{1\text{-}2,eq} = \Delta i_{act,1\text{-}2,eq} = \Delta g_{1\text{-}2,eq} = 0.05$. In this figure, a resistive symmetrical transient short-circuit, with a short-circuit voltage $u_{CC} = 0.15$ and a duration of 2 s, is introduced at second 3. Since the short-circuit is purely resistive, the maximum achievable differences are $\Delta p_{1\text{-}2,\max} = 0$ and $\Delta i_{act,1\text{-}2,\max} = 0$ according to (23) and (36). This can be observed in Fig. 11 where the differences $\Delta p_{1\text{-}2}$ and $\Delta i_{act,1\text{-}2}$ remain close to zero during the disturbance. As a result, there are no equilibrium points when using P-f and I_{act}-f droops and the phase differences $\Delta\delta_{P\text{-}f}$ and $\Delta\hat{I}_{I_{act}\text{-}f}$ increase continuously meaning that the inverters become desynchronized. In contrast, the G-f droop provides the system with synchronization stability maintaining the inverters synchronized with the same $\Delta\delta_{G\text{-}f}$ as in normal operation, despite the harshness of the short-circuit. Therefore, thanks to the proposed G-f droop, the inverters feed the short-circuit with the highest level of current.

When the fault is cleared at second 5, although the voltage at the PCC initially increases with P-f and I_{act}-f droops, the inverters continue limiting the current due to the high phase difference between them. As a result, the inverters remain desynchronized after the fault and the phase difference increases leading to the decrease of the voltage at the PCC. In contrast, the system does not present this undesired response when using the G-f droop and the voltage at the PCC recovers immediately after the fault as shown in Fig. 11. This is possible thanks to the low phase difference maintained by the G-f droop during the short-circuit, making the activation of the current limitation unnecessary.

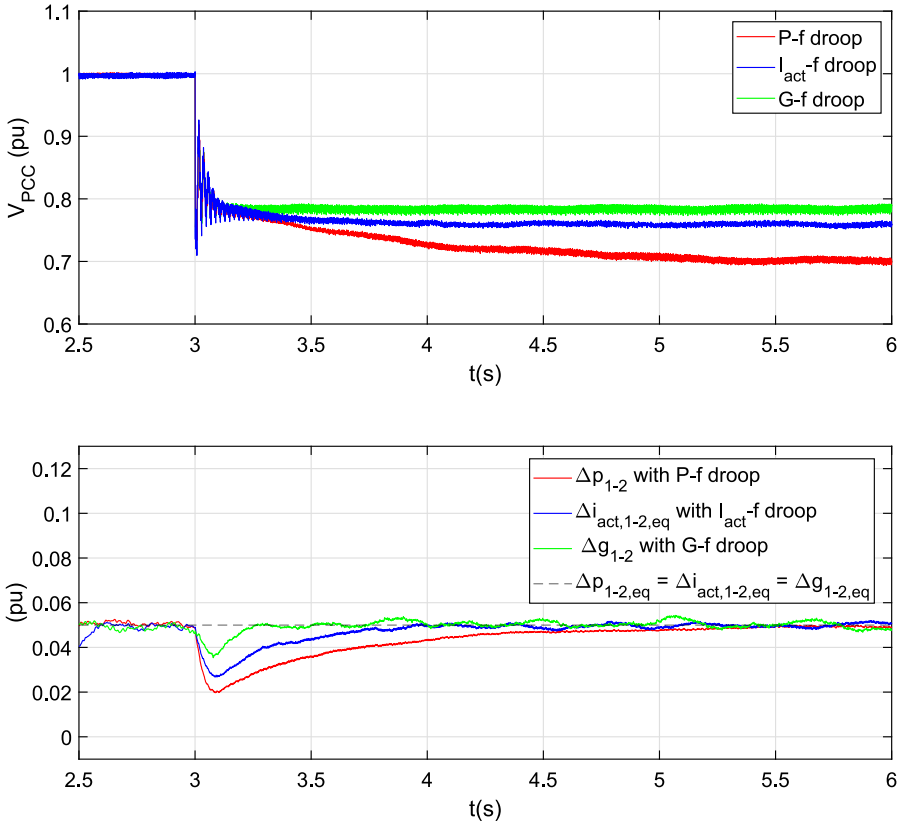

Fig. 13. Time-domain HIL waveforms of the inverter-based stand-alone microgrid with P-f droop (blue), I_{act}-f droop (red) and G-f droop (green), requiring $\Delta p_{1\text{-}2,eq} = \Delta i_{act,1\text{-}2,eq} = \Delta g_{1\text{-}2,eq} = 0.05$ in the presence of a 25 % permanent overload, $y_{load} = 2.5$, with $\phi_{load} = 5°$. (For interpretation of the references to colour in this figure legend, the reader is referred to the web version of this article.)

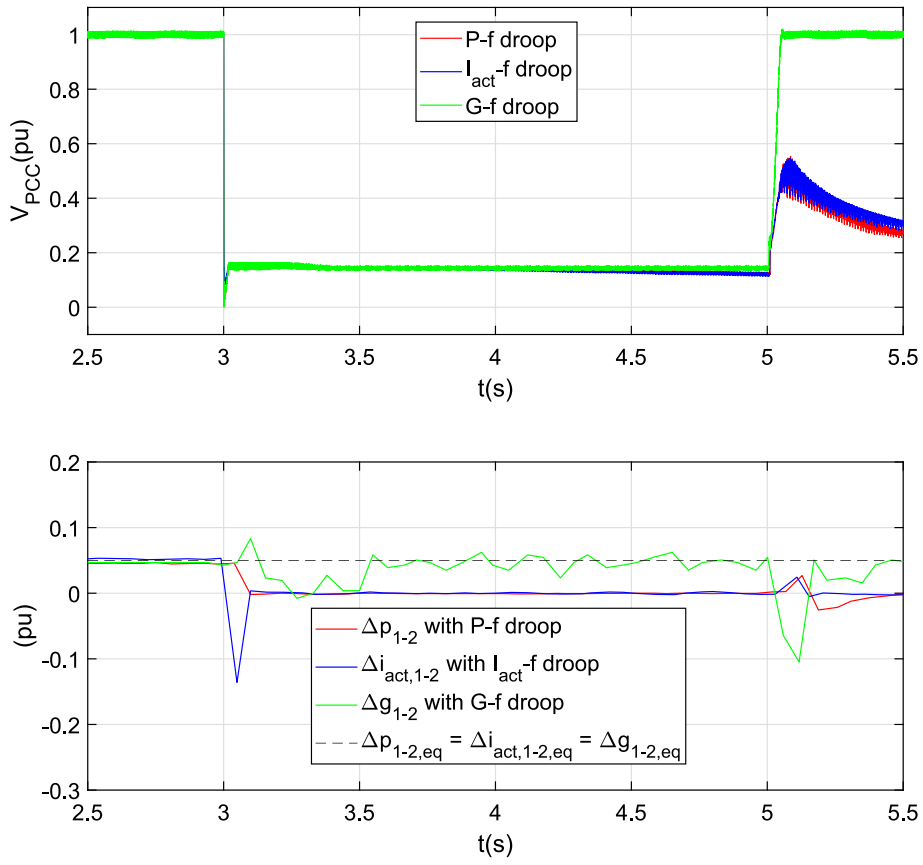

Fig. 14. Time-domain HIL waveforms of the inverter-based stand-alone microgrid with *P-f* droop (red), I_{act}-*f* droop (blue) and *G-f* droop (green), requiring $\Delta p_{1\text{-}2,eq} = \Delta i_{act,1\text{-}2,eq} = \Delta g_{1\text{-}2,eq} = 0.05$ in the presence of a resistive symmetrical transient short-circuit with $u_{CC} = 0.15$ and a duration of 2 s (from normal operating to short-circuit and reverse). (For interpretation of the references to colour in this figure legend, the reader is referred to the web version of this article.)

The simulation results show the synchronization stability problems of the system during current limitation when the frequency of the inverters is controlled by means of the *P-f* droop or the I_{act}-*f* droop. Additionally, the superior performance of the *G-f* droop is validated, ensuring the synchronization stability of the system irrespective of the operating conditions.

6. HIL validation

Hardware-in-the-Loop (HIL) experiments based on the OPAL-RT platform have been carried out to further verify the performance of the microgrid during current limitation when using the *P-f* droop, the I_{act}-*f* droop and the proposed *G-f* droop. The HIL platform shown in Fig. 12 includes the HIL simulator and the circuit boards and controllers (DSPs) of two commercial inverters INGECON SUN STORAGE Power 1500 V. In this way, the inverter-based stand-alone microgrid, presented in Section 2, is tested considering the same parameters for the power and control stages as in the simulations. For validation, two cases of those presented in Section 5 were replicated testing the system with the frequency droop controls, and again imposing $f_{0,1} = f_{0,2}$ and including an estimation offset that leads to $\Delta p_{1\text{-}2,eq} = \Delta i_{act,1\text{-}2,eq} = \Delta g_{1\text{-}2,eq} = 0.05$.

Figure 13 shows the time-domain HIL waveforms of the stand-alone microgrid for the three frequency droop controls. Initially, both inverters were synchronized, feeding a load of $y_{load} = 1$ in normal operation, $v_{PCC} = 1$, and the corresponding differences are $\Delta p_{1\text{-}2} = \Delta i_{act,1\text{-}2} = \Delta g_{1\text{-}2} = 0.05$. In the same way as the simulation (see Fig. 9), at second 3 an overload with $\phi_{load} = 5^{\circ}$ and $y_{load} = 2.5$ (25 % overload) was introduced, transferring the inverters to current limitation and provoking a decrease in the PCC voltage. As can be observed, the system is transiently stable in all three cases, but the response is different depending on the method employed. With regard to the transitory response, the *G-f* droop is the fastest method to reach the equilibrium point, while the *P-f* droop is the slowest. At the equilibrium point, the best steady-state operation of the system also occurs with the *G-f* droop, which maintains the highest V_{PCC} during the overload, specifically, $v_{G\text{-}f} = 0.783$, $v_{I_{act}\text{-}f} = 0.761$ and $v_{P\text{-}f} = 0.702$.

Similarly, Fig. 14 shows the time-domain HIL waveforms of the stand-alone microgrid for the three frequency droop controls. In this figure, a resistive symmetrical transient short-circuit, with a short-circuit voltage $u_{CC} = 0.15$ and a duration of 2 s, was introduced at second 3, in the same way as the simulation (see Fig. 11). When the resistive short-circuit occurs, the differences $\Delta p_{1\text{-}2}$ and $\Delta i_{act,1\text{-}2}$ drop immediately to zero since the maximum achievable differences are $\Delta p_{1\text{-}2,\max} = \Delta i_{act,1\text{-}2,\max} = 0$ for $\phi_{load} = 0^{\circ}$ according to (24) and (37). As a result, the required differences $\Delta p_{1\text{-}2,eq} = \Delta i_{act,1\text{-}2,eq} = 0.05$ cannot be achieved meaning that the system response when using the *P-f* and I_{act}-*f* droops is unstable during the short-circuit and the inverters become desynchronized, which is in line with the simulation results shown in Fig. 11. Nevertheless, according to the HIL results, the phase differences between inverters with *P-f* and I_{act}-*f* droops undergo a slightly higher increase than in the simulation causing the PCC voltage to decrease to a lower value during the fault and to vary differently during the initial instants of fault recovery. In relation to the response with *G-f* droop, the system is transiently stable during the short-circuit, given that the equilibrium point with $\Delta g_{1\text{-}2} = 0.05$ is reached, maintaining the inverters synchronized. Furthermore, the low phase difference maintained by the *G-f* droop makes it possible to recover the PCC voltage immediately after the fault.

The results obtained by means of the HIL tests validate the transitory and steady-state responses obtained in the simulation results and

confirm the superior performance of the proposed *G-f* droop.

7. Conclusions

In this article, the synchronization stability analysis of an inverter-based stand-alone microgrid in the presence of overloads and short-circuits at the PCC is first carried out considering two conventional methods to control the frequency of the inverters, the *P-f* and I_{act}-*f* droops. This study shows the instability problems of the *P-f* and I_{act}-*f* droops that do not guarantee the continued synchronization of the microgrid inverters under all possible operating conditions. In this way, the stability boundaries of the system were obtained depending on the method employed and as a function of the frequency setpoints, offset errors and load parameters. The study makes it possible to conclude that the performance of the *P-f* and I_{act}-*f* droops is somewhat affected by the operating conditions due to the strong voltage influence on the active power and active current.

To dictate the inverter frequency, this article then proposes the *G-f* droop, which consists in implementing the frequency droop control by using a variable defined as the equivalent conductance seen by each inverter. As has been demonstrated, the equivalent conductance scarcely depends on the voltage and the *G-f* droop exhibits the same performance irrespective of the operating conditions, always ensuring the synchronization stability of the stand-alone microgrid. Furthermore, this method maintains the inverters synchronized with low phase differences also in the presence of overloads and short-circuits, giving the system considerable capabilities such as ensuring the maximum voltage and current at the PCC or facilitating voltage recovery after the disturbance. The superior performance of the *G-f* droop compared to the *P-f* and I_{act}-*f* droops was validated by simulation and HIL results, also showing an enhanced dynamic system response.

Declaration of Competing Interest

The authors declare that they have no known competing financial interests or personal relationships that could have appeared to influence the work reported in this paper.

Data availability

The data that has been used is confidential.

Acknowledgements

The authors would like to acknowledge the ongoing support of Ingeteam Power Technology.

References

[1] Zhong Q-C, Hornik T. Control of power inverters in renewable energy and smart grid integration. Wiley; 2012.
[2] Bevrani H, François B, Ise T. Microgrid dynamics and control. John Wiley & Sons; 2017.
[3] Hatziargyriou N, Asano H, Iravani R, Marnay C. Microgrids. IEEE Power Energy Mag 2007;5(4):78–94.
[4] Rocabert J, Luna A, Blaabjerg F, Rodríguez P. Control of power converters in AC microgrids. IEEE Trans Power Electron 2012;27(11):4734–49.
[5] Xin H, Zhao R, Zhang L, Wang Z, Wong KP, Wei W. A decentralized hierarchical control structure and self-optimizing control strategy for FP type DGs in islanded microgrids. IEEE Trans Smart Grid 2015;7(1):3–5.
[6] Guerrero JM, Vasquez JC, Matas J, De Vicuña LG, Castilla M. Hierarchical control of droop-controlled AC and DC microgrids—a general approach toward standardization. IEEE Trans Ind Electron 2010;58(1):158–72.
[7] Zhong Q-C, Zeng Y. Universal droop control of inverters with different types of output impedance. IEEE Access 2016;4:702–12.
[8] Bevrani H, Ise T, Miura Y. Virtual synchronous generators: a survey and new perspectives. Int J Electr Power Energy Syst 2014;54:244–54.
[9] Liu J, Miura Y, Ise T. Comparison of dynamic characteristics between virtual synchronous generator and droop control in inverter-based distributed generators. IEEE Trans Power Electron 2015;31(5):3600–11.
[10] Simpson-Porco JW, Dörfler F, Bullo F. Synchronization and power sharing for droop-controlled inverters in islanded microgrids. Automatica 2013;49(9):2603–11.
[11] Qoria T, Li C, Oue K, Gruson F, Colas F, Guillaud X. Direct AC voltage control for grid-forming inverters. J Power Electron 2020;20(1):198–211.
[12] Wei B, Marzàbal A, Perez J, Pinyol R, Guerrero JM, Vásquez JC. Overload and short-circuit protection strategy for voltage source inverter-based UPS. IEEE Trans Power Electron 2019;34(11):11371–82.
[13] Gkountaras A, Dieckerhoff S, Sezi T. Evaluation of current limiting methods for grid forming inverters in medium voltage microgrids. IEEE Energy Convers Congress Exposition (ECCE) 2015;2015:1223–30.
[14] Eskandari M, Savkin AV. On the impact of fault ride-through on transient stability of autonomous microgrids: nonlinear analysis and solution. IEEE Trans Smart Grid 2021;12(2):999–1010.
[15] Lou G, Yang Q, Gu W, Zhang J. An improved control strategy of virtual synchronous generator under symmetrical grid voltage sag. Int J Electr Power Energy Syst 2020;121:106093.
[16] Zarei SF, Mokhtari H, Ghasemi MA, Blaabjerg F. Reinforcing fault ride through capability of grid forming voltage source converters using an enhanced voltage control scheme. IEEE Trans Power Deliv 2018;34(5):1827–42.
[17] Qoria T, Gruson F, Colas F, Kestelyn X, Guillaud X. Current limiting algorithms and transient stability analysis of grid-forming VSCs. Electr Power Syst Res 2020;189:106726.
[18] Shi K, Song W, Xu P, Liu R, Fang Z, Ji Y. Low-voltage ride-through control strategy for a virtual synchronous generator based on smooth switching. IEEE Access 2017;6:2703–11.
[19] Shuai Z, Huang W, Shen C, Ge J, Shen ZJ. Characteristics and restraining method of fast transient inrush fault currents in synchronverters. IEEE Trans Ind Electron 2017;64(9):7487–97.
[20] Erdocia J, Urtasun A, Marroyo L. Dual Voltage-current control to provide grid-forming inverters with current limiting capability. IEEE J Emerg Sel Top Power Electron Emerging Appl Power Electron Dev Econ 2022;10(4):3950–62.
[21] De Brabandere K, Bolsens B, den Keybus J, Woyte A, Driesen J, Belmans R. A voltage and frequency droop control method for parallel inverters. IEEE Trans. Power Electron. 2007;22(4):1107–15.
[22] Wang X, Taul MG, Wu H, Liao Y, Blaabjerg F, Harnefors L. Grid-synchronization stability of converter-based resources—an overview. IEEE Open J Ind Appl 2020;1:115–34.
[23] Xin H, Huang L, Zhang L, Wang Z, Hu J. Synchronous instability mechanism of Pf droop-controlled voltage source converter caused by current saturation. IEEE Trans Power Syst 2016;31(6):5206–7.
[24] Qoria T, Gruson F, Colas F, Denis G, Prevost T, Guillaud X. "Critical clearing time determination and enhancement of grid-forming converters embedding virtual impedance as current limitation algorithm. IEEE J Emerg Sel Top Power Electron 2019;8(2):1050–61.
[25] Cheema KM, Milyani AH, El-Sherbeeny AM, El-Meligy MA. Modification in active power-frequency loop of virtual synchronous generator to improve the transient stability. Int J Electr Power Energy Syst 2021;128:106668.
[26] Oureilidis KO, Demoulias CS. A fault clearing method in converter-dominated microgrids with conventional protection means. IEEE Trans Power Electron 2015;31(6):4628–40.
[27] Belila A, Amirat Y, Benbouzid M, Berkouk EM, Yao G. Virtual synchronous generators for voltage synchronization of a hybrid PV-diesel power system. Int J Electr Power Energy Syst 2020;117:105677.
[28] Huang L, Xin H, Wang Z, Zhang L, Wu K, Hu J. Transient stability analysis and control design of droop-controlled voltage source converters considering current limitation. IEEE Trans. Smart Grid 2017;10(1):578–91.
[29] Li Z, Hu J, Chan KW. A new current limiting and overload protection strategy for droop-controlled voltage-source converters in islanded AC microgrids under grid faulted conditions. IEEE Energy Conv Congr Exposition (ECCE) 2020;2020:3888–93.
[30] Du W, Chen Z, Schneider KP, Lasseter RH, Pushpak Nandanoori S, Tuffner FK, et al. A comparative study of two widely used grid-forming droop controls on microgrid small-signal stability. IEEE J Emerg Sel Top Power Electron 2020;8(2):963–75.
[31] Cheema KM. A comprehensive review of virtual synchronous generator. Int J Electr Power Energy Syst 2020;120:106006.
[32] Pei X, Kang Y. Short-circuit fault protection strategy for high-power three-phase three-wire inverter. IEEE Trans Ind Informatics 2012;8(3):545–53.
[33] Pawar B, Batzelis EI, Chakrabarti S, Pal BC. Grid-forming control for solar PV systems with power reserves. IEEE Trans Sustain Energy 2021;12(4):1947–59.
[34] Urtasun A, Barrios EL, Sanchis P, Marroyo L. Frequency-based energy-management strategy for stand-alone systems with distributed battery storage. IEEE Trans. Power Electron. 2015;30(9):4794–808.
[35] Urtasun A, Sanchis P, Marroyo L. State-of-charge-based droop control for stand-alone AC supply systems with distributed energy storage. Energy Convers Manag 2015;106:709–20.
[36] Lu X, Sun K, Guerrero J, Huang L. SoC-based dynamic power sharing method with AC-bus voltage restoration for microgrid applications. In: in IECON 2012–38th Annual Conference on IEEE Industrial Electronics Society; 2012. p. 5677–82.